J. Fluid Mech. (1976), *vol.* 73, *part* 1, *pp.* 9–32
Printed in Great Britain

The calculation of near-wake flows

By S. B. POPE AND J. H. WHITELAW
Department of Mechanical Engineering, Imperial College, London

(Received 23 April 1975)

Calculated flow properties are compared with measurements obtained in two-dimensional isothermal wakes with and without recirculation. The equations of continuity and momentum were solved numerically together with equations which formed a turbulence model. Calculations were made using three turbulence models: the first comprised transport equations for turbulence kinetic energy and the rate of turbulence dissipation; the second and third comprised equations for the rate of turbulence dissipation and two forms of Reynolds-stress equations characterized by different redistribution terms. The results show that, for wakes without recirculation, the particular turbulence model is less important than the boundary condition assumed in the plane of the trailing edge of the body; though the Reynolds-stress models do, of course, provide a better representation of the individual normal stresses. In the case of wakes with recirculation, both the length of the recirculation region and the rate of spread of the downstream wake are underestimated. The second discrepancy is particularly evident and appears to stem from the form of the dissipation equation. A suggestion for improving the modelling of this equation is provided together with necessary justification.

1. Introduction

The efforts described in this paper stem from early attempts to calculate the flow properties downstream of turbulent blunt-body stabilized flames and the observation that, although the measurements and calculations were in disagreement, it was impossible to decide which was incorrect. As a consequence, it was decided to examine the data available for isothermal wakes, with and without recirculating flow, and to attempt to determine the source of the disagreement: it was presumed that available measurements in isothermal flows were sufficiently more reliable than those in combusting flow to allow the assessment. The early calculations were performed with a two-equation turbulence model incorporating an isotropic-viscosity assumption. This formulation assumed that the anisotropy of the Reynolds stresses is determined locally and that the principal axes of stress and strain are coincident. Theoretical arguments and experimental evidence show that the first assumption becomes progressively worse as the flow departs from homogeneity and the second is not appropriate to any real flow. As a result, the present calculations are based on a five-equation model incorporating separate transport equations for each of the non-zero Reynolds stresses. They are compared with values obtained from a two-equation model to demonstrate the extent to which the inappropriate isotropic-viscosity assumption influences the results.

A survey of experimental information in the literature relating to near-wake flows, with and without recirculation, showed that available data were in short supply. The papers by Chevray (1968) and Chevray & Kovasznay (1969) reported velocity and velocity correlation measurements obtained in the wakes downstream of an ellipsoid and a thin flat plate respectively: in both cases, the region of recirculation immediately downstream of the body was negligibly small but the axial velocity gradients were of the same order of magnitude as the radial gradients. Carmody (1964) reported similar measurements downstream of a disk. In this case the region of recirculating flow was extensive and covered by the measurements. The recent measurements of Durão & Whitelaw (1974) and Durão (1975, private communication) are also helpful in this connexion since they relate to the wake downstream of an annular jet: they were obtained using a laser-Doppler anemometer, rather than the hot wires of previous authors, and this helps to remove any bias which might result from the consideration of hot-wire data alone. The calculation procedure solves differential equations in elliptic form. It requires, therefore, boundary conditions for each equation on the whole perimeter of the solution domain. As will be shown, the data reported in the above papers do not provide complete information on these boundary conditions, and consequently their influence must be quantified.

The contributions of this paper are described in the following sections entitled, respectively, 'Equations and turbulence models', 'Solution algorithm', 'Predictions' and 'Discussion'. The paper closes with a summary of the more important conclusions. The section on equations and turbulence models is necessary to present and explain the models used for the present calculations: the basis for the turbulence models is not new but they have not all previously been presented or explained in the form appropriate to recirculating flow and elliptic equations. The boundary conditions and wall functions are also presented and discussed in this section. Because of the use of a Reynolds-stress closure within the framework of a numerical scheme for the solution of elliptic equations, the algorithm of the numerical procedure of Patankar & Spalding (1973) had to be modified significantly; these modifications are described in the section on the solution algorithm. The results of the calculations are presented in the last major section and are compared with the results of the four experimental investigations referred to earlier. Thus the ability of the various turbulence models to represent near-wake flows with and without recirculation is established and the sensitivity to unknown boundary conditions quantified.

2. Equations and turbulence models

Three sets of equations were solved to obtain the results presented in § 4. They are quoted here in terms of Cartesian tensors and expanded in the appendix in Cartesian and cylindrical-polar co-ordinates. The continuity and momentum equations are common to each set, i.e.

$$\partial(\rho U_i)/\partial x_i = 0 \tag{1}$$

and

$$\partial(\rho U_i U_j + \rho\overline{u_i u_j} + p\delta_{ij})/\partial x_i = 0. \tag{2}$$

The equations which make up the three turbulence models are as follows.

(I) Two-equation model:

$$\frac{\partial}{\partial x_i}(\rho U_i k) = \frac{\partial}{\partial x_i}\left(\frac{\mu_{\text{eff}}}{\sigma_k}\frac{\partial k}{\partial x_i}\right) + P - \rho\epsilon, \tag{3}$$

$$\frac{\partial}{\partial x_i}(\rho U_i \epsilon) = \frac{\partial}{\partial x_i}\left(\frac{\mu_{\text{eff}}}{\sigma_\epsilon}\frac{\partial \epsilon}{\partial x_i}\right) + \frac{\epsilon}{k}(C_{\epsilon 1}P - C_{\epsilon 2}\rho\epsilon), \tag{4}$$

$$\mu_{\text{eff}} = C_\mu \rho k^2/\epsilon, \quad P = -\rho\overline{u_i u_j}\,\partial U_i/\partial x_j, \quad k = \tfrac{1}{2}\overline{u_i u_i},$$

$$-\rho\overline{u_i u_j} = \mu_{\text{eff}}\left(\frac{\partial U_i}{\partial x_j} + \frac{\partial U_j}{\partial x_i}\right) - \tfrac{2}{3}\rho k \delta_{ij}.$$

The Reynolds-stress models used differ only in the redistribution term. Their common form is

$$\frac{\partial}{\partial x_l}(\rho U_l \overline{u_i u_j}) = \frac{\partial}{\partial x_l}\left(C_s \rho \frac{k}{\epsilon}\overline{u_l u_m}\frac{\partial \overline{u_i u_j}}{\partial x_m}\right) + P_{ij} + R_{ij} - \tfrac{2}{3}\rho\epsilon\delta_{ij}, \tag{5}$$

$$\frac{\partial}{\partial x_l}(\rho U_l \epsilon) = \frac{\partial}{\partial x_l}\left(C_\epsilon \rho \frac{k}{\epsilon}\overline{u_l u_m}\frac{\partial \epsilon}{\partial x_m}\right) + \frac{\epsilon}{k}(C_{\epsilon 1}P - C_{\epsilon 2}\rho\epsilon), \tag{6}$$

$$P_{ij} = -\rho\overline{u_i u_l}\frac{\partial U_j}{\partial x_l} - \rho\overline{u_j u_l}\frac{\partial U_i}{\partial x_l}.$$

The redistribution terms R for the two models are as follows.

(II) Reynolds-stress model, first redistribution term:

$$R_{ij} = -\rho C_{\phi 1}\epsilon(\overline{u_i u_j}/k - \tfrac{2}{3}\delta_{ij}) - C_{\phi 2}(P_{ij} - \tfrac{2}{3}P\,\delta_{ij}).$$

(III) Reynolds-stress model, second redistribution term:

$$\begin{aligned} R_{ij} = {} & -\rho C_{\phi 1}\epsilon(\overline{u_i u_j}/k - \tfrac{2}{3}\delta_{ij}) - B_1(P_{ij} - \tfrac{2}{3}P\delta_{ij}) \\ & - B_2\rho k(\partial U_i/\partial x_j + \partial U_j/\partial x_i) - B_3(G_{ij} - \tfrac{2}{3}P\delta_{ij}), \end{aligned}$$

where

$$G_{ij} = -\rho\overline{u_i u_l}\,\partial U_l/\partial x_j - \rho\overline{u_j u_l}\,\partial U_l/\partial x_i,$$

$$B_1 = \tfrac{1}{11}(C_{\phi 2} + 8), \quad B_2 = \tfrac{1}{55}(30C_{\phi 2} - 2), \quad B_3 = \tfrac{1}{11}(8C_{\phi 2} - 2).$$

The common part of the redistribution terms was proposed by Rotta (1951). The second parts were proposed by Naot, Shavit & Wolfshtein (1970) and by Launder, Reece & Rodi (1975) respectively. The constants used are given in table 1.

Model	C_μ	σ_k	C_ϵ	$C_{\epsilon 1}$	$C_{\epsilon 2}$	$C_{\phi 1}$	$C_{\phi 2}$	C_s	C_ϵ	Number of constants
I	0·09	1·0	1·3	1·45	1·9	—	—	—	—	5
II	—	—	—	1·45	1·9	2·5	0·4	0·25	0·15	6
III	—	—	—	1·45	1·9	1·5	0·4	0·25	0·15	6

TABLE 1

The co-ordinate systems, either Cartesian or cylindrical polar, were orientated such that the plane or axis of symmetry was given by $x_2 = 0$ and that $\partial/\partial x_3 = 0$. The boundary conditions appropriate to these equations and the present calculations were

all quantities specified function of x_2 on $x_1 = 0$,

$\partial/\partial x_1$ of all quantities $= 0$ as $x_1 \to \infty$,

$U_2 = \overline{u_1 u_2} = 0$, $\partial/\partial x_2$ of all other quantities $= 0$ on $x_2 = 0$,

$\overline{u_1 u_2} = 0$, all other quantities take free-stream values except U_2, whose gradient is known from the continuity equation, as $x_2 \to \infty$.

Where possible, experimental boundary conditions were used for the boundary $x_1 = 0$ but, as will be seen, they were not always available.

In the near-wall region, the following functions were added to the equations and boundary conditions and precluded the need for fine-grid calculations in that region:

$$\tau_w = \frac{U_P}{y_P}\frac{\mu y_P^+}{\kappa^{-1}\ln(E y_P^+)}, \quad \text{where} \quad y_P^+ \equiv \rho(k_P C_\mu^{\frac{1}{2}})^{\frac{1}{2}} y_P/\mu,$$

$$\epsilon_P = (C_\mu^{\frac{1}{2}} k_P)^{\frac{3}{2}}/\kappa y_P,$$

$$\int_0^{y_P} \epsilon\, dy = (C_\mu^{\frac{1}{2}} k_P)^{\frac{3}{2}} \frac{1}{\kappa} \ln(E y_P^+),$$

diffusion $= 0$ for all Reynolds stresses.

τ_w is the wall shear stress and μ the laminar viscosity. The subscript P refers to the grid node next to the wall and κ and E are the wall-law constants, with values of 0·4 and 8·8.

These three turbulence models have been examined, in boundary-layer form and in the context of free flows, by Launder *et al.* (1972) and further related explanations and discussion have been provided by Launder *et al.* (1975) and by Launder & Spalding (1972). Only the two-equation model has, to date, been applied to recirculating flows and then without a detailed assessment of its abilities (e.g. Khalil & Whitelaw 1974). It is known that the two-equation closure, incorporating an isotropic-viscosity hypothesis, is unable to represent the properties of some boundary-layer flows, e.g. asymmetric channel flow, swirling flows and the flow in a square duct, and the same deficiencies may be expected in

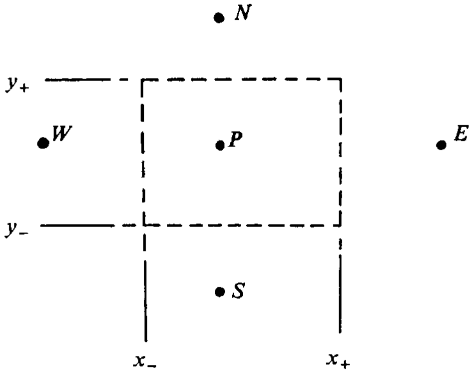

FIGURE 1. Finite-difference grid.

recirculating flows. The Reynolds-stress closure is probably as complete a set of equations as can be formulated and solved without resorting to guess work: it is particularly appropriate to recirculating flows because the Reynolds stresses are not related to local quantities but calculated from appropriate conservation equations.

Of course, the dissipation, diffusion and redistribution terms in (3)–(6) are not calculated in their exact form and imprecisions undoubtedly arise from these sources. This point will be discussed further in § 4.

3. Solution algorithm

Equations (1) and (2) and any one of the turbulence models together with boundary conditions and auxiliary relations form a closed set of equations. Equations (2)–(6) may be written in the common form

$$\frac{\partial}{\partial x}(\rho U\phi)+\frac{1}{r}\frac{\partial}{\partial y}(r\rho V\phi)-\frac{\partial}{\partial x}\left(\Gamma_x\frac{\partial\phi}{\partial x}\right)-\frac{1}{r}\frac{\partial}{\partial y}\left(r\Gamma_y\frac{\partial\phi}{\partial y}\right)=S_\phi, \tag{7}$$

where $\mathbf{x}=(x,y,z)$, $\mathbf{U}=(U,V,W)$ while $r\equiv 1$ for Cartesian co-ordinates and $r\equiv y$ for cylindrical-polar co-ordinates. Equations of this form were solved by finite-difference means as described below.

Figure 1 shows part of a finite-difference grid where the values of ϕ are assumed known at the nodes P, N, S, E and W. Equation (7) may be integrated over the indicated control volume to give

$$\left[\int_{y_-}^{y_+} r\left(\rho U\phi-\Gamma_x\frac{\partial\phi}{\partial x}\right)dy\right]_{x_-}^{x_+}+\left[r\int_{x_-}^{x_+}\left(\rho V\phi-\Gamma_y\frac{\partial\phi}{\partial y}\right)dx\right]_{y_-}^{y_+}=\int_{y_-}^{y_+}\int_{x_-}^{x_+} rS_\phi\,dx\,dy. \tag{8}$$

The following finite-difference approximations may be made:

$$\int_{y_-}^{y_+} r\rho U\phi\,dy\bigg|_{x_+}\approx \tfrac{1}{2}(\phi_P+\phi_E)(\rho U)_{x+}\int_{y_-}^{y_+} r\,dy = C_{x+}(\phi_P+\phi_E), \tag{9}$$

$$\int_{y_-}^{y_+} r\Gamma_x\frac{\partial\phi}{\partial x}dy\bigg|_{x_+}\approx \frac{\phi_E-\phi_P}{x_E-x_P}(\Gamma_x)_{x+}\int_{y_-}^{y_+} r\,dy = D_{x+}(\phi_E-\phi_P), \tag{10}$$

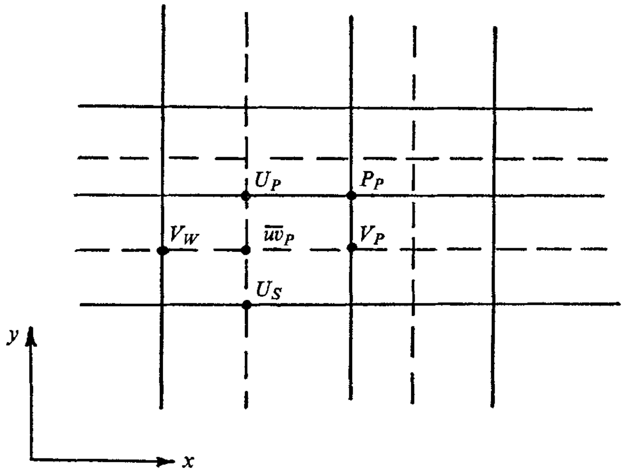

FIGURE 2. Juxtaposition of grid nodes.

$$\int_{y-}^{y+}\int_{x-}^{x+} rS_\phi\,dx\,dy \approx (S_\phi)_{xp}\int_{y-}^{y+}\int_{x-}^{x+} r\,dy\,dx = (S_\phi)_{xp}\,\text{vol}, \tag{11}$$

with $A_E = D_{x+}+C_{x+}$, $A_W = D_{x-}-C_{x-}$ etc.;† substituting (9)–(11) into (8) gives

$$\phi_P(A_N+A_S+A_E+A_W) = A_N\phi_N+A_S\phi_S+A_E\phi_E+A_W\phi_W+(S_\phi)_{xp}\,\text{vol}. \tag{12}$$

If the pressure is known, then (12), written for each variable at each grid node, yields a closed set of algebraic equations. However, there is no guarantee that the resultant velocity field would satisfy the continuity relation (1). The two problems of determining the pressure and satisfying continuity are overcome by adjusting the pressure field so as to satisfy continuity. The details of this aspect of the procedure have been reported elsewhere (Patankar & Spalding 1973) but it should be noted that it requires a specific juxtaposition of the velocity and pressure nodes; see figure 2. All other equations are normally solved at the pressure nodes.

A significant modification of the numerical scheme of Patankar & Spalding (1973) was found necessary in the solution of the Reynolds-stress equations. In the case of model I the term $\partial(\rho\overline{u_iu_j})/\partial x_i$ may be expressed as a diffusion term, i.e. $\Gamma_x = \Gamma_y = \mu_{\text{eff}}$ in (7). With the solution of the Reynolds-stress equations, the strong link between the stress and rate of strain is not retained within the same equation and, to provide numerical stability, it was found necessary to locate the shear-stress nodes in the manner indicated in figure 2. This arrangement helps to preserve the link referred to above. Thus a small increase in $\overline{uv}_P$ from its correct value results in increases in U_P and V_P and decreases in U_S and V_W; as a consequence, $\partial U/\partial y$ and $\partial V/\partial x$ increase at the $\overline{uv}_P$ node. The effect of these increased velocity gradients is to decrease, through the source term in the $\overline{u_iu_j}$ equation, the value of $\overline{uv}_P$ towards its correct value.

---

† The finite-difference coefficients are modified according to a hybrid scheme (Gosman *et al.* 1968, p. 229).

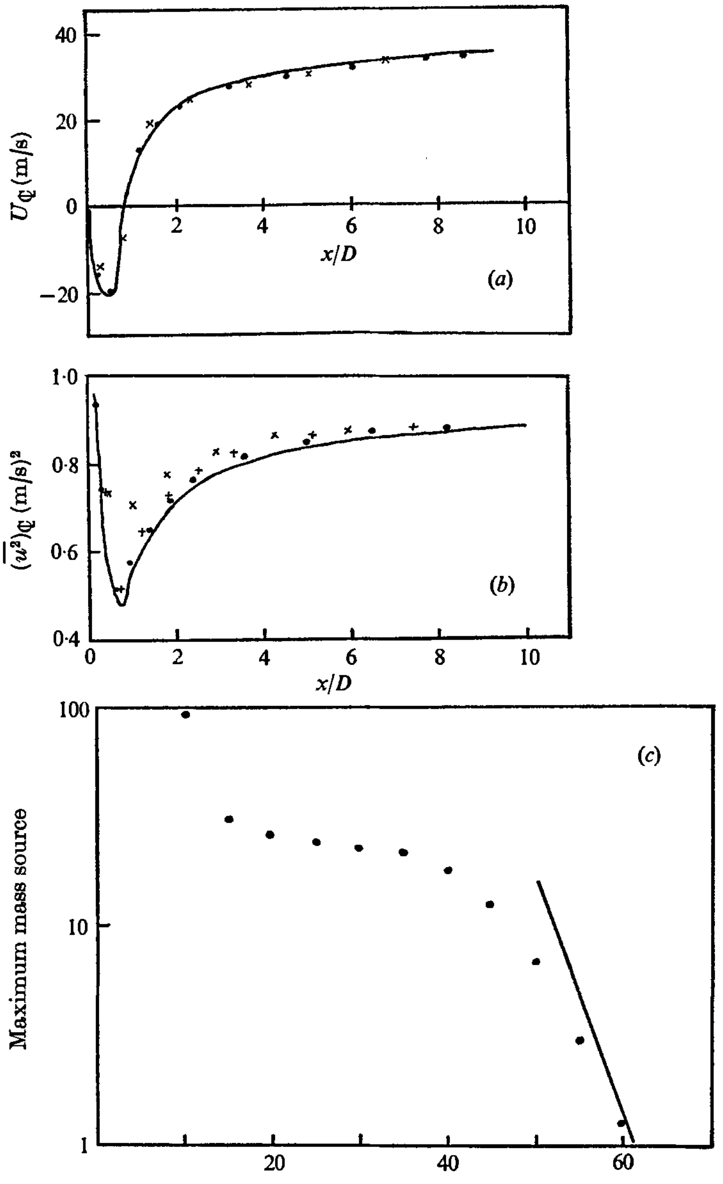

FIGURE 3. Solution-algorithm test calculations. (*a*) $U_{℄}$ *vs*. x/D. (*b*) $(\overline{u^2})_{℄}$ *vs*. x/D. (*c*) Maximum mass source *vs*. number of iterations. (*a*), (*b*) ×, 10 × 10 grid; +, 14 × 14 grid; ●, 18 × 18 grid; ——, 26 × 26 grid.

In the procedure described above, and unlike some alternative schemes, there are no special difficulties associated with axes of symmetry provided that the finite-difference approximations (9)–(11) are altered to take account of the information that, in a region close to an axis, the shear stress is proportional to distance from the axis. In the present scheme, (9) was replaced by

$$\int_0^{y+} r\rho U\overline{uv}\,dy\bigg|_{x+} \approx \int_0^{y+} r^2\rho U\left(\frac{\overline{uv}}{r}\right)_P dy\bigg|_{x+} \approx \frac{(\overline{uv})_P+(\overline{uv})_E}{2r_P}(\rho U)_{x+}\int_0^{y+} r^2\,dy \qquad (13)$$

and corresponding alterations made to (10) and (11).

Since this procedure differed significantly from that employed for equations other than those for the Reynolds stress, tests were carried out to ensure that, for any grid size below some limit, the solutions were the same. Figure 3 shows calculated values of the mean axial velocity and the corresponding normal stress along the centre-line of a wake similar to that of Carmody. The results show that the numerical accuracy is reasonable even with a 14 × 14 grid. The calculated values of Reynolds stresses at other locations in the field showed similar accuracy.

The finite-difference equations were solved iteratively by a Fortran program on a CDC 6600 digital computer. The storage and time requirements of the program were 16000 + 20 words per grid node and 0·0025 s/iteration per grid node respectively.

For a 20 × 20 grid this resulted in a storage requirement of 24000 words and a time for each iteration of 1 s. The measure of convergence used was the maximum of the mass sources required at each node to satisfy the continuity equation: for a converged solution this is zero. The maximum mass source was plotted against the number of iterations for a 10 × 10 grid on figure 3. The performance of the procedure was virtually the same as that based on the isotropic-viscosity hypothesis except that the time required to obtain a converged solution increased by about 50 %. This increase in time is due to the fact that the procedure solves for eight dependent variables rather than for five.

4. Predictions

The calculated values of the various dependent variables are presented together with the experimental data referred to in the introduction. It should be remembered, however, that both the calculated and measured values are subject to possible errors.

The *measurements of Chevray* (1968) included values of the mean axial and radial velocities and all the non-zero Reynolds stresses at various locations downstream of his ellipsoid. The inlet values of each dependent variable except dissipation were, therefore, available from experiment and the dissipation was assumed to be equal to the production of turbulent kinetic energy.

The calculated profiles of U/U_E are shown on figure 4 and those of $\overline{uv}/U_E^2$ on figure 5. The figures show the results of calculations obtained with each of the

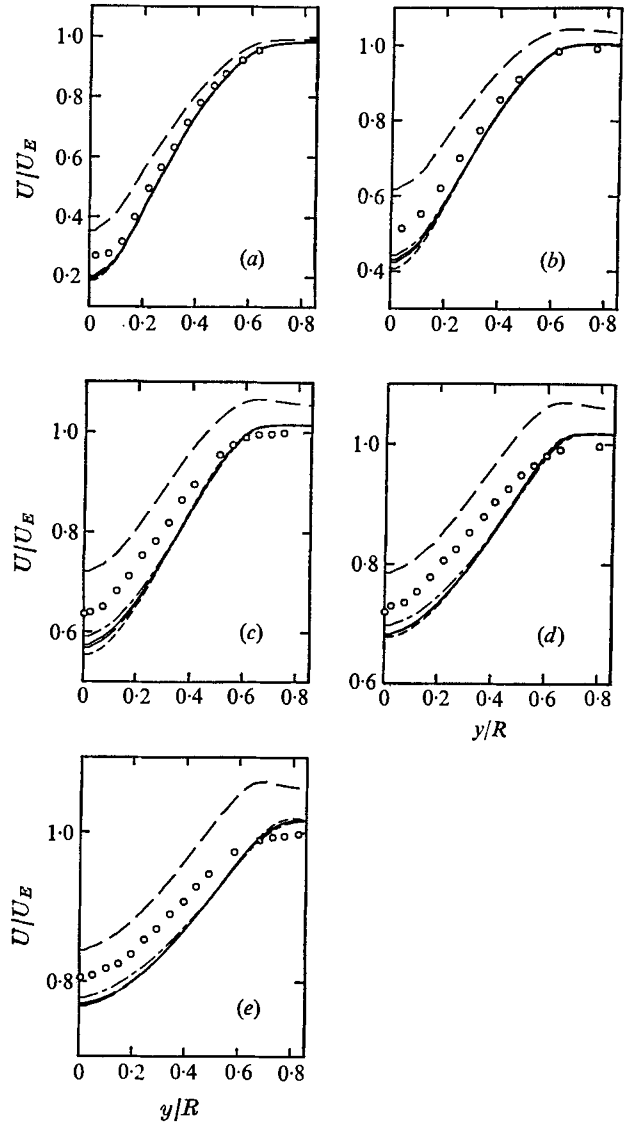

FIGURE 4. Flow of Chevray (1968). U/U_E *vs.* y/R. ○, measurements; ----, model I; ——, model II; ——, model III; — — — —, model III with inlet velocity V doubled; — · —, model III with inlet ϵ decreased by 20 %.

	(a)	(b)	(c)	(d)	(e)
x/R	0·5	2·0	6·0	12·0	18·0

three turbulence models and demonstrate the effect of a 20 % decrease in the initial values of ϵ and of doubling the initial values of V. The experimental data are indicated on the figures for comparison purposes.

It can be seen from figure 4 that each of the three models results in values of the mean velocity which are sensibly identical except in the vicinity of the symmetry axis, where small differences occur. In general, the non-dimensional

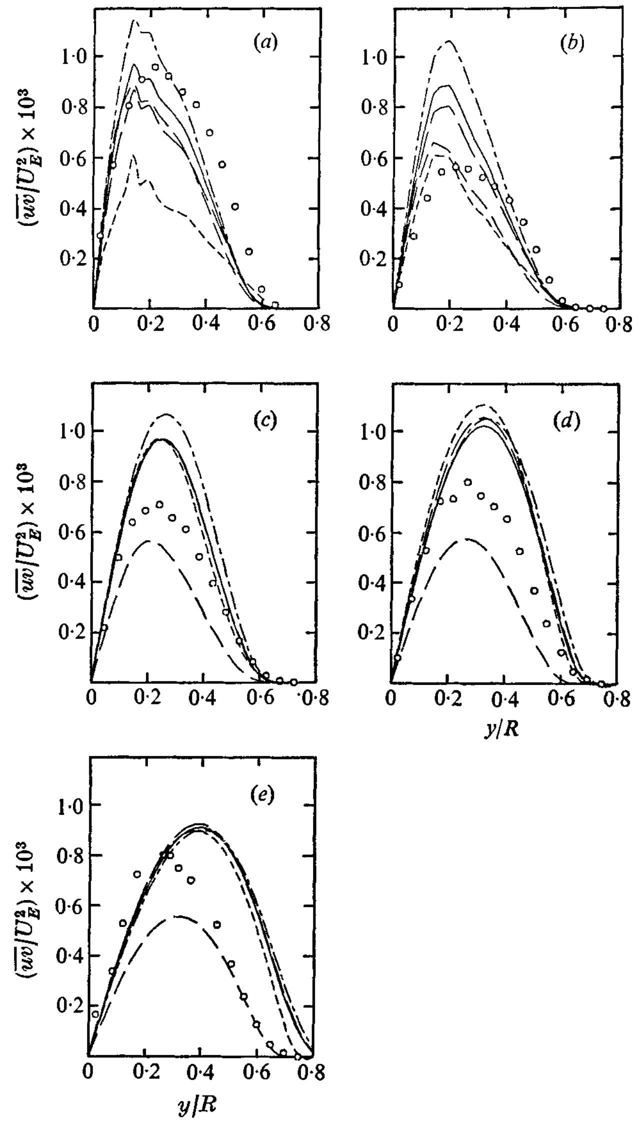

FIGURE 5. Flow of Chevray (1968): $\overline{uv}/U_E^2$ vs. y/R. Notation as in figure 4.

	(a)	(b)	(c)	(d)	(e)
x/R	1·0	2·0	6·0	12·0	18·0

calculated velocity values are lower than the measurements: the comparison suggests that the mixing is too low in the vicinity of the symmetry axis and that this suppresses the development of the wake. However, the calculated shear stress is greater than the measured values, thus refuting this supposition and suggesting instead that the measurements do not satisfy the axial momentum equation. This discrepancy could stem from the measured values of V used as inlet conditions in the calculation: it is undoubtedly possible that these values are subject to errors, which could be as large as a factor of two. For this reason,

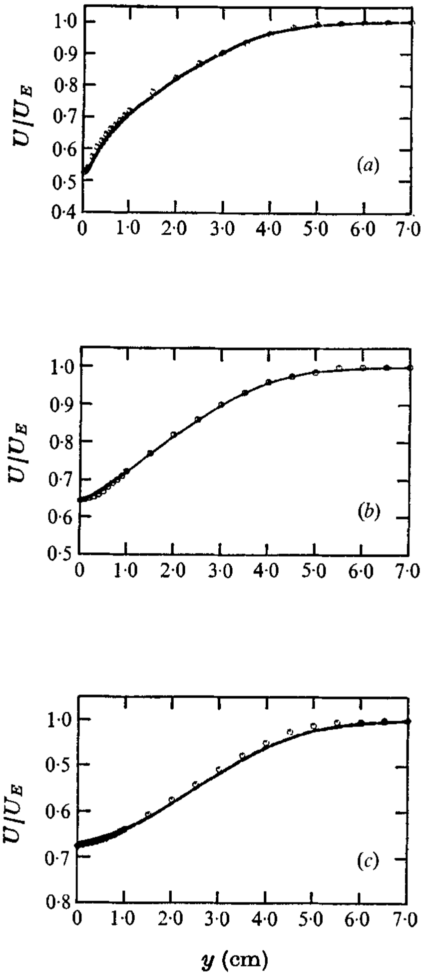

FIGURE 6

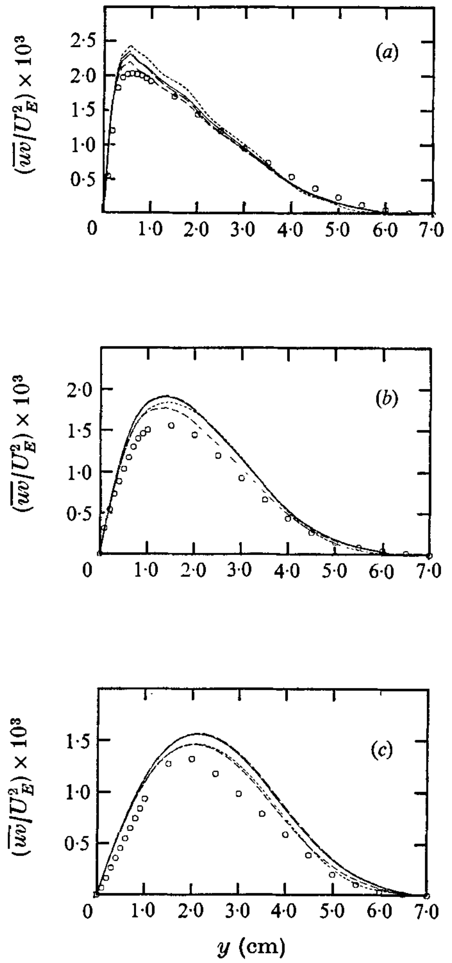

FIGURE 7

FIGURE 6. Flow of Chevray & Kovasznay (1969): U/U_E *vs.* y. ○, measurements; ----, model I; – – –, model II; ——, model III; — — —, model III with inlet ϵ increased by 20 %. (*a*) $x = 5$ cm. (*b*) $x = 20$ cm. (*c*) $x = 50$ cm.

FIGURE 7. Flow of Chevray & Kovasznay (1969): $\overline{uv}/U_E$ *vs.* y. Notation as in figure 6. (*a*) $x = 5$ cm. (*b*) $x = 20$ cm. (*c*) $x = 50$ cm.

the calculations were repeated with initial V values which were twice the measured values. As can be seen, the U profiles at downstream locations became larger than the measured values.

The comparison between measured and calculated values of the non-dimensional shear stress, shown in figure 5, again shows that all models result in similar trends to the measurements. In the upstream region the shear stress predicted by model I is far less than that predicted by the Reynolds-stress models. This reflects the fact that model I takes no account of the convection of the individual stresses. Once again, the influence of the initial V profile is large and

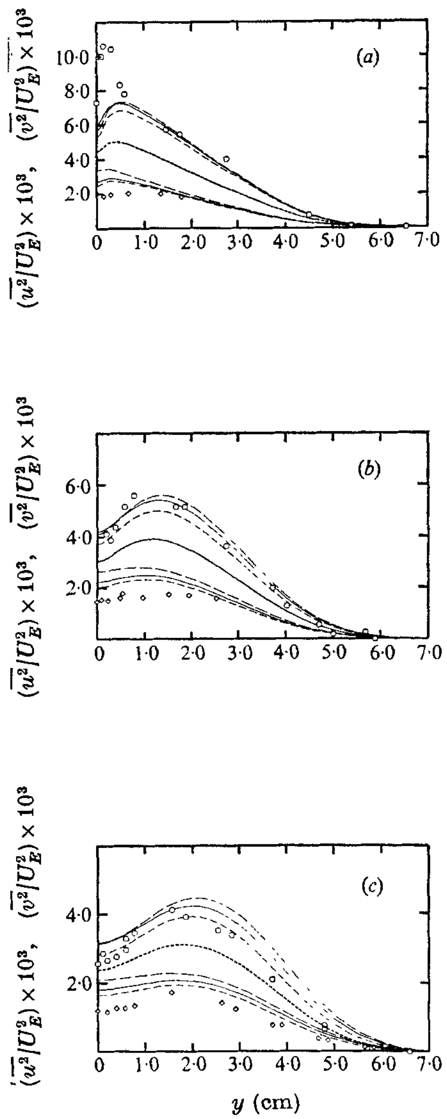

FIGURE 8. Flow of Chevray & Kovasznay (1969). Measurements: ○, $\overline{u^2}/U_E^2$; ◇, $\overline{v^2}/U_E^2$. Other notation as in figure 6. (a) $x = 5$ cm. (b) $x = 20$ cm. (c) $x = 50$ cm.

does not allow any quantitative assessment of the ability of the three models to predict shear stress.

The *measurements of Chevray & Kovasznay* (1969) were obtained downstream of a thin flat plate, and consequently the uncertainty in the V velocity at the trailing edge (assumed zero) and hence its influence can be expected to be significantly less than in the data of Chevray (1968). The reported data are for the mean axial velocity, $\overline{u^2}$, $\overline{v^2}$ and $\overline{uv}$ and it can be anticipated that the precision of measurements in this later investigation will not be less than in the former. The inlet values of $\overline{w^2}$ were taken from the data of Klebanoff (1954) while, again, the dissipation was equated to the production of turbulent kinetic energy. Figure 6 allows a comparison between measured and calculated values of the mean axial velocity, shear-stress values being shown on figure 7 and normal stresses on figure 8.

As was the case with the flow configurations of Chevray, the three models result in calculated values of the mean velocity which are virtually identical. On this occasion, however, the agreement between measurements and calculations is excellent. The predictions of shear stress are adequate and, once again, do not allow any model to be identified as a clear improvement over any other: this is made particularly clear by the differences which result from a 20% increase in the assumed initial values of ϵ. The agreement between the measurements and calculations in figures 6 and 7 is certainly sufficiently good to provide confidence in the initial values used for the calculations. The differences between the measured values of $\overline{u^2}$ and $\overline{v^2}$ and those calculated with each of the models is, therefore, particularly significant. It can readily be seen that model III provides calculated values which are in good agreement with experiment; model II is slightly less satisfactory and model I is inadequate. The influence of the assumed initial ϵ profile does not alter this conclusion.

The *measurements of Carmody* (1964) are also extensive and are particularly relevant to blunt-body stabilized flames in that they were performed downstream of a disk (or radius R) in a free stream (with velocity U_E). The separated nature of this flow provides a greater test of the present turbulence models than the flows of Chevray and Chevray & Kovasznay but it should be remembered that it also presents a more formidable measurement problem. Figures 9 and 10 give comparisons between measured and calculated mean values: figure 9 is concerned with the growth rate and centre-line velocity and figure 10 with velocity profiles at downstream locations. Figure 11 presents shear-stress profiles and figure 12 normal-stress profiles.

The inlet value of the axial velocity was taken from the data. The radial velocity quoted by the author was evaluated from the continuity equation and consequently is subject to a large error. The values used were obtained by solving for the flow upstream of the disk, assuming it to be inviscid and using the measured axial velocity as a boundary condition. The validity of this approach was confirmed by the observation that, at the inlet, the dynamic head calculated from the measured axial velocity and pressure and the predicted radial velocity was nearly constant. The inlet values of the normal stresses were set at $0{\cdot}002U_E^2$, while the dissipation was set through the length scale with $l/R = 0{\cdot}03$. These nominal free-stream values may be expected not to influence the calculations very much as a great deal of turbulence is produced in the region immediately downstream of the disk.

The results displayed on figure 9 show that, with the inlet conditions stated above, none of the models results in values of the half-width or of the centre-line velocity which are in close agreement with the measurements. The differences resulting from the three models and from doubling the inlet value of the dissipation are small compared with those resulting from an 80% decrease in the values of the radial inlet velocity or from an augmentation of the turbulence close to

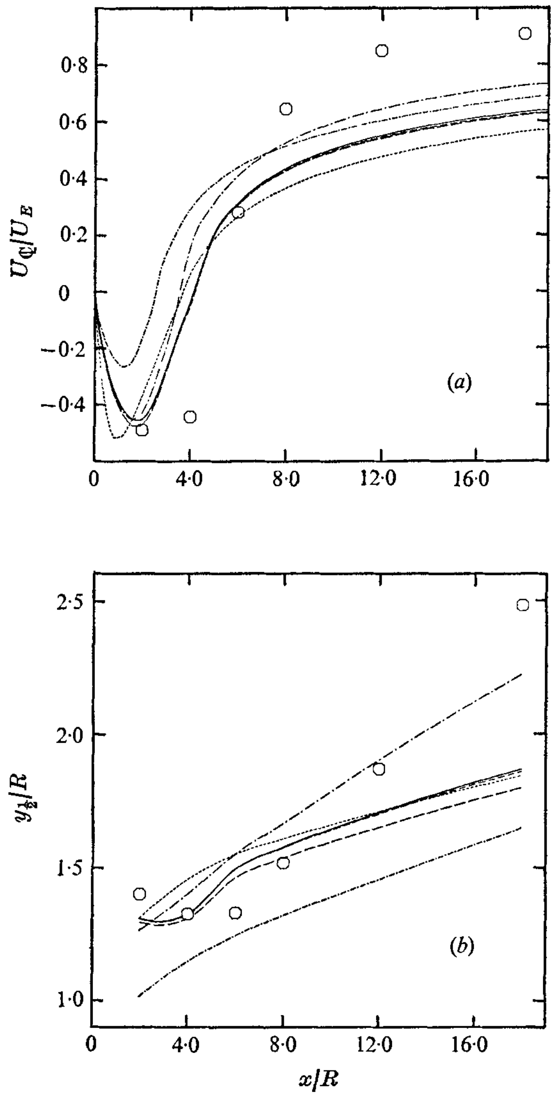

FIGURE 9. Flow of Carmody (1964): (a) $U_{\mathbb{C}}/U_E$ *vs.* x/R; (b) $\overline{u^2}/U_E^2$ *vs.* x/R. - - - - -, model I; — — —, model II; ———, model III; —·—, model III with inlet V velocity decreased by 80 %; — — — —, model III with inlet ϵ doubled; ——·——, model III with augmented turbulence at inlet.

the baffle tip. The decreased velocity corresponds to that suggested by Carmody while augmenting the turbulence close to the baffle tip by setting

$$(\overline{u^2})^{\frac12}/U_E = (\overline{v^2})^{\frac12}/U_E = (\overline{w^2})^{\frac12}/U_E = 0{\cdot}14 \quad \text{and} \quad l/R = 0{\cdot}4 \quad \text{for} \quad 1{\cdot}0 < y/R < 2{\cdot}0$$

(i.e. $0 < U/U_E < 0{\cdot}95$) is intended to simulate a thick shear layer in that region. As can be seen from figure 9, the decrease in V (from a maximum of $0{\cdot}74\,U_E$) and the increase in turbulence intensity have large influences on the predicted growth rates and centre-line velocity distribution. The poor agreement between the

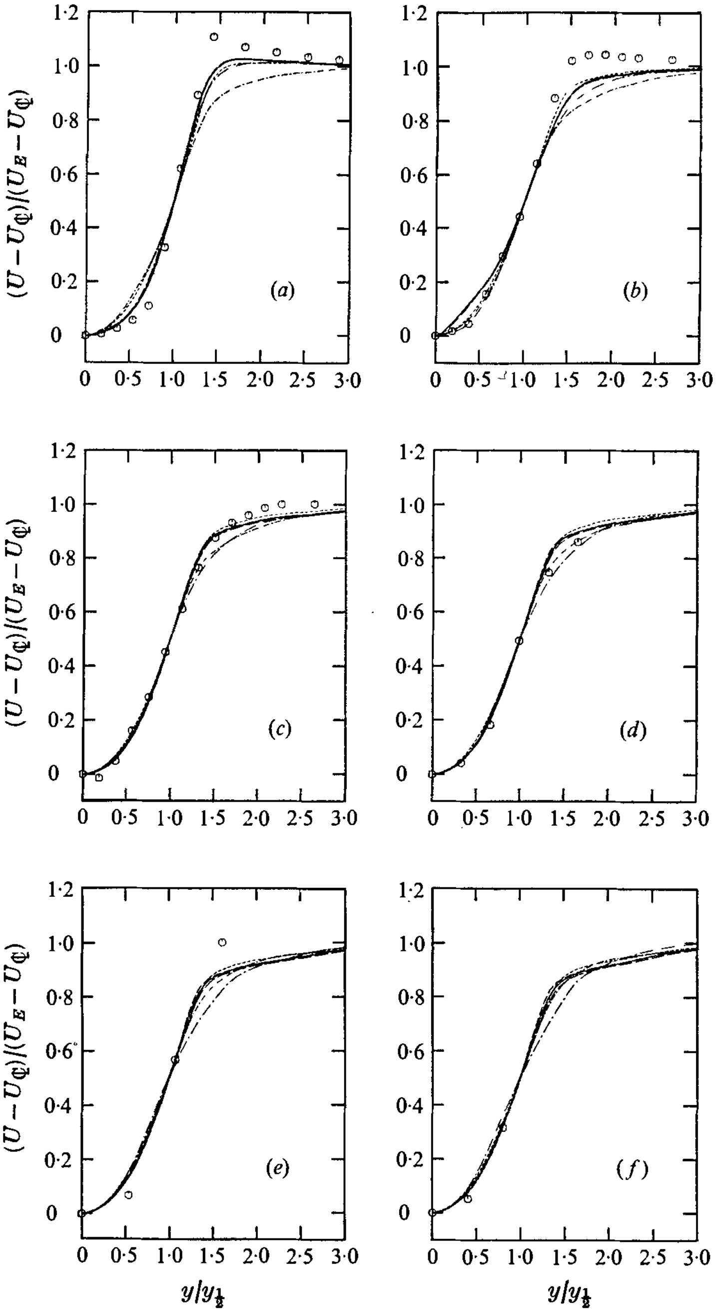

FIGURE 10. Flow of Carmody (1964): $(U-U_{\text{℄}})/(U_E-U_{\text{℄}})$ *vs.* y/R. Notation as in figure 9.

	(a)	(b)	(c)	(d)	(e)	(f)
x/R	2·0	4·0	6·0	8·0	12·0	18·0

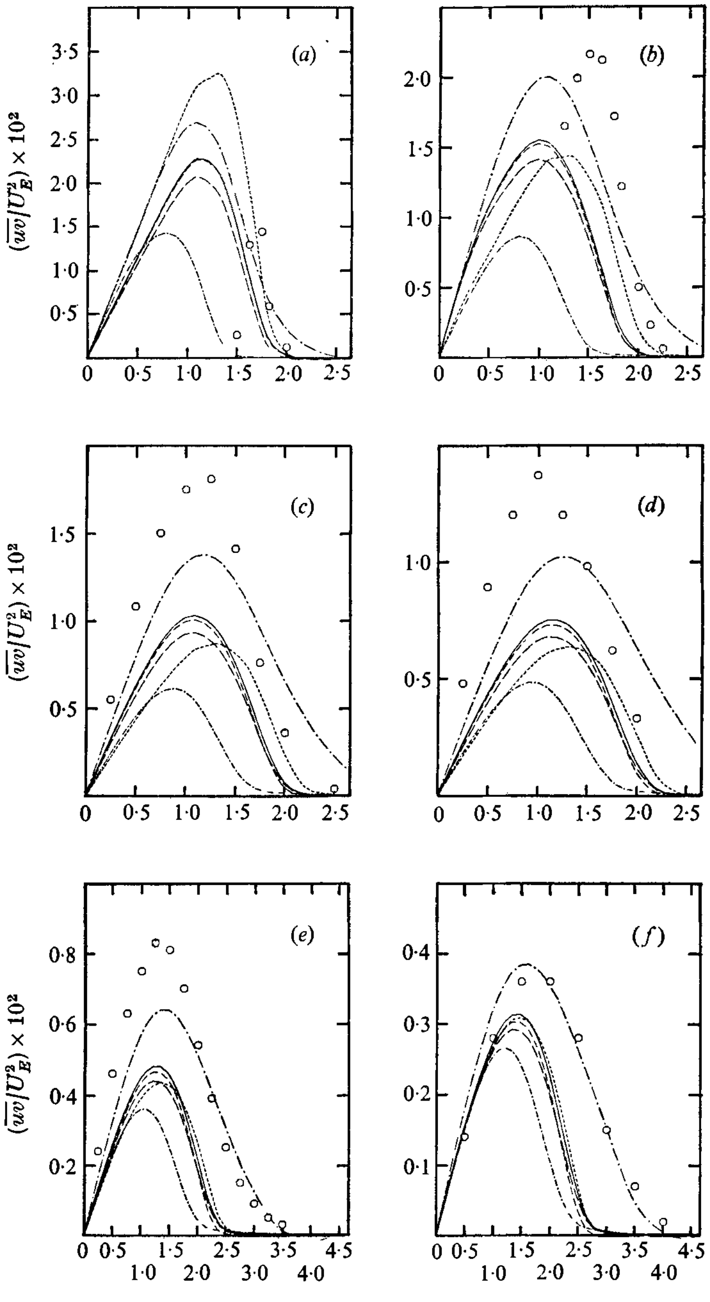

FIGURE 11. Flow of Carmody: $\overline{uv}/U_E^2$ *vs.* y/R. Notation as in figure 9.

	(*a*)	(*b*)	(*c*)	(*d*)	(*e*)	(*f*)
x/R	2·0	4·0	6·0	8·0	12·0	18·0

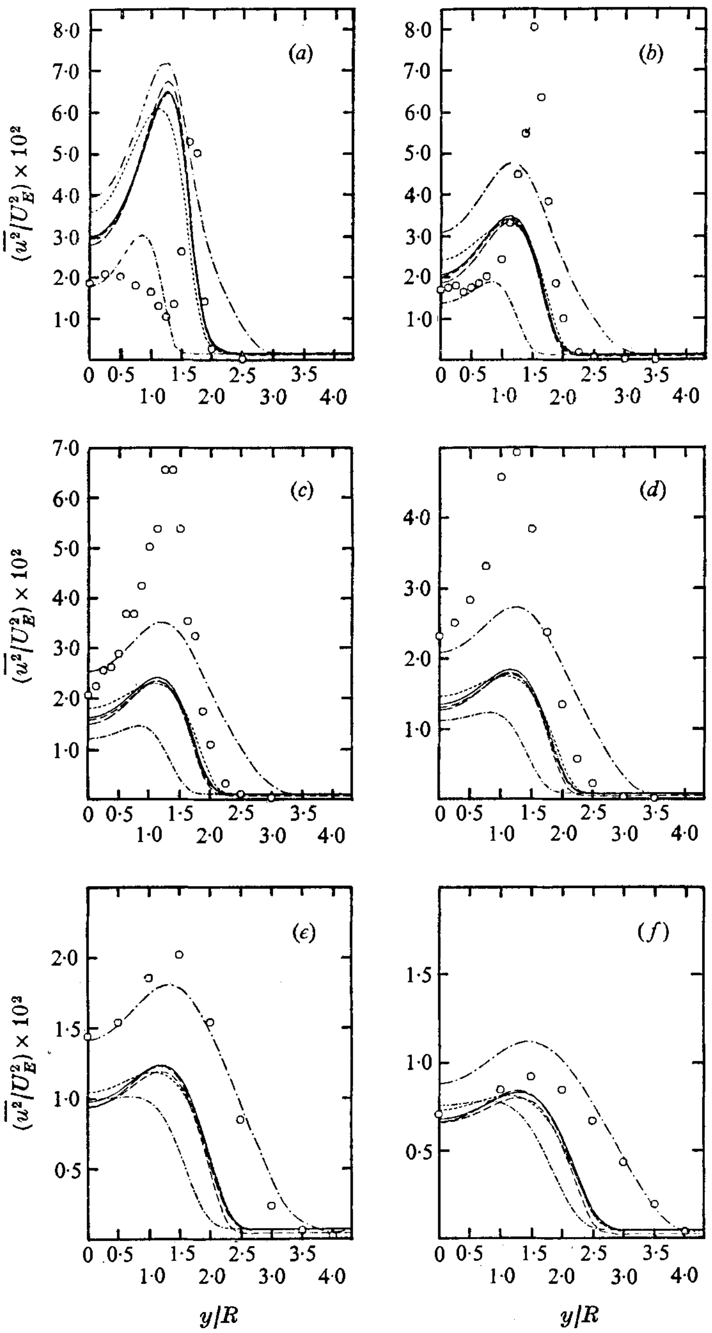

FIGURE 12. Flow of Carmody: $\overline{u^2}/U_E^2$ *vs.* y/R. Notation as in figure 9.

	(a)	(b)	(c)	(d)	(e)	(f)
x/R	2·0	4·0	6·0	8·0	12·0	18·0

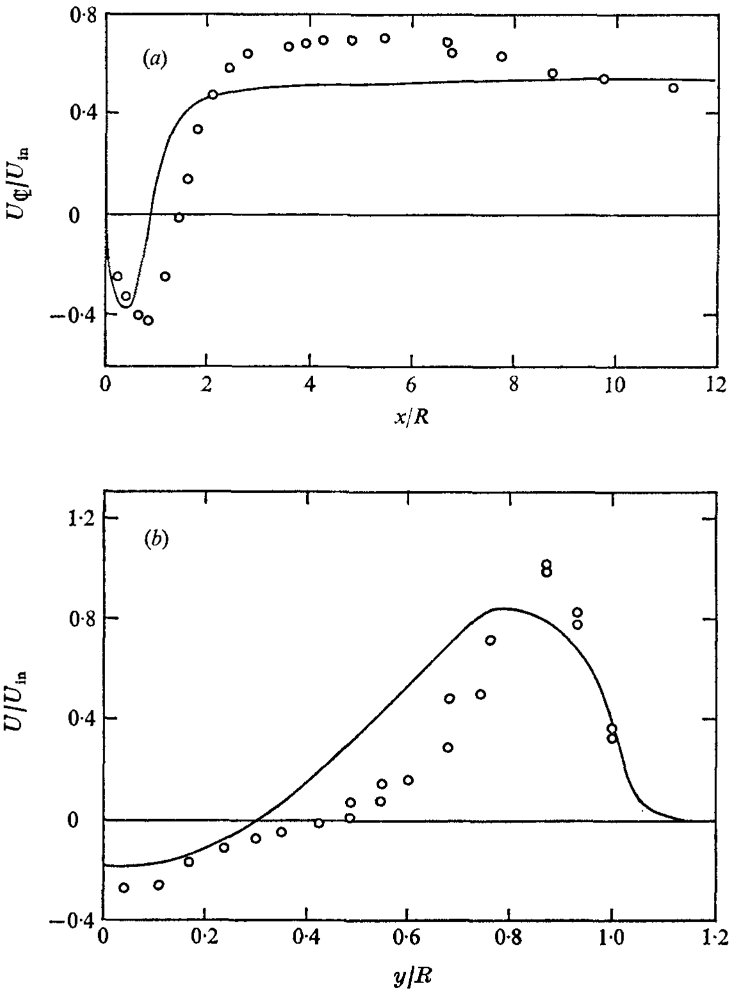

FIGURE 13. Flow of Durão & Whitelaw (1974): (a) $U_{¢}/U_{in}$ *vs.* x/R; (b) U/U_{in} *vs.* y/R. ○, measurements; ——, predictions (all models).

measurements and the predictions with V decreased confirms that the present estimate is more reliable. The predictions with the higher turbulence intensity at the inlet give a spreading rate $dy_{\frac{1}{2}}/dx$ increased from 0·025 to 0·05. However, these values must be compared with the experimental value of 0·1 and the difference cannot reasonably be attributed to uncertainties in the boundary conditions. The two Reynolds-stress models fare better than model I in the recirculation zone but, bearing in mind experimental difficulties in this region and the sizeable discrepancies downstream, no model may be distinguished as being better than the others.

The shear-stress results in figure 10 demonstrate differences between the results of the three models but, once again, the influences of V and turbulence initial conditions are larger than those of the models. Clearly the augmented initial turbulence intensity and model III lead to results which are in remarkably good agreement with experiment, particularly in the downstream region where the measurements are more accurate.

The normal-stress results in figure 11 allow the same tentative conclusion as figure 10. In addition, however, the measurements reveal inexplicable behaviour in the upstream region and must be considered suspect. Also, models II and III will always be more successful for the calculation of normal stresses since they are not made equal in plane shear flow as with model I.

The *measurements of Durão & Whitelaw* (1974) pertain to an annular jet, the inner radius of the jet being 0·72 times the outer radius R. Close to the outlet of the jet a region of reversed flow occurred in the vicinity of the centre-line, thus initiating a wake which decayed further downstream. The outer region of the flow resembled a decaying jet, and for $x/R > 100$, where the wake had vanished, the measurements show self-preserving jet profiles. Upstream of the nozzle there was a contraction to ensure that the turbulence intensity at the exit was small.

Figure 13 shows measurements and predictions of the centre-line velocity and the velocity profile at $x/R = 0{\cdot}6$. The predictions of the centre-line velocity are virtually the same for each turbulence model and show similar discrepancies to those encountered with Carmody's data. The length of the recirculation zone is again underpredicted. The almost constant predicted value of $U_{\mathbb{C}}/U_{\mathrm{in}}$ further downstream is due to a balance between the decay of the wake (tending to increase the velocity) and the spreading of the flow (tending to decrease the velocity). Further measurements by Durão (1975, private communication) show that the wake decays more quickly than is predicted, thus accounting for the different shapes of the two curves.

The predicted velocity profiles are again virtually the same for each of the turbulence models and show a significant discrepancy with the measurements.

5. Discussion

The previous section shows that significant discrepancies exist between measurements and predictions and may be attributed both to inaccurate measurements, leading to erroneous boundary conditions, and to deficiencies in the turbulence models.

An approach which would overcome the first problem would be to increase the size of the solution domain so that known boundary conditions could be applied upstream of the body. This approach is, in principle, advantageous but may present difficulties in practice. The correct representation of the boundary-layer flows around the solid body requires a finite-difference grid with a comparatively larger number of nodes. This is expensive in terms of computer time and may still not produce calculated values of flow properties at the downstream plane of the solid body which are more precise than the measurements available at present. The present calculations quantify the precision with which the flow around the solid body must be calculated.

Two particular defects which result from the turbulence models are evident in the prediction of the recirculating flow. The length of the region of recirculation is underpredicted as is the rate at which the wake decays. The same defects have been observed by Vasilić (1975, private communication), who used model I to predict the two-dimensional flow over a thin obstruction mounted normal to a plane surface.

In order to understand the more serious defect, the underprediction of the spreading rate, it is necessary to consider the nature of round-wake flows, a useful discussion of which is given by Rodi (1972). Round wakes are potentially 'approximately self-similar', that is, as $U_{\mathbb{C}}/U_E \rightarrow 1$, appropriately normalized mean quantities and the spreading parameter $S \equiv U_E/(U_E - U_{\mathbb{C}})\, dy_{\frac{1}{2}}/dx$ may become independent of x. Rodi (1972) considered nine sets of experimental data and concluded that round wakes do become self-similar. However, unlike all commonly encountered free shear flows, the profiles of mean quantities, and in particular the spreading parameter, are strongly dependent upon the way in which the flow is initiated. Of particular interest here are the values of S for the flows measured by Chevray (1968) and Carmody (1964), which are $S = 0{\cdot}105$ and $S = 0{\cdot}8$ respectively. The non-uniqueness of self-similar round wakes may be attributed to the fact that they are weak-shear flows, that is the effect of local velocity gradients upon the Reynolds stresses is up to an order of magnitude less than the effect of dissipation. The consequences of these observations for the turbulence models are twofold. First, unless the flow around the recirculation zone is predicted accurately the downstream predictions are unlikely to be correct, and second, the dissipation equation will govern the spreading rate almost entirely.

Although the discrepancies in the predictions of the recirculation zones are not as great nor as well substantiated as those in the spreading rate, the above arguments indicate that great precision is required in the recirculation zone if the wake is to be correctly represented. In the recirculation region the Reynolds-stress models offer the potential advantages over a two-equation model that the differential transport of Reynolds stresses is permitted and that the need for an effective-viscosity hypothesis is obviated. The effect of allowing for the differential transport of the Reynolds stresses is difficult to assess. Certainly, the gross features of the flows considered here are not dependent on this transport in contrast to asymmetric channel flow or annular pipe flow for example. However, the results demonstrate that the Reynolds-stress closures are necessary to represent the different magnitudes of the stresses and that they result in slightly better predictions of the mean velocity. This advantage might also be obtained with an effective-viscosity closure if the transport of Reynolds stresses was assumed proportional to their magnitudes. Unlike the isotropic formulation, the effective-viscosity hypothesis deduced from the Reynolds-stress equation with the above assumption (Pope 1975) can provide a realistic modelling of all the Reynolds stresses and, in addition, makes C_μ a function of the rate of strain and rotation.

The form of the dissipation equation is common to the three models, and since it is based on unproven assumptions, may be a source of error both in the near and far wake. It was developed and tested in two-dimensional near-equilibrium boundary-layer flows and free shear flows where only one velocity gradient was significant. Thus it is not surprising that the net source term was modelled as a linear function of the only non-zero independent invariant of the velocity-gradient tensor. Since, in general, there are five independent invariants there is clearly scope for improvement. Bradshaw (1973) and Priddin (1975, private communication) have also criticized the form of the dissipation equation, particularly in relation to flows with streamline curvature, which will also be poorly represented by the present source term. In the present context, the rotation invariant $\Omega \equiv (\partial U_i/\partial x_j - \partial U_j/\partial x_i)^2$ is of particular interest: in a two-dimensional shear flow without streamline curvature it is equal to the rate-of-strain invariant $S \equiv (\partial U_i/\partial x_j + \partial U_j/\partial x_i)^2$. Thus the dimensionless parameter $(\Omega - S)/(\Omega + S)$, which is unity for solid-body rotation, zero for parallel shear flow and -1 for plane strain, may be introduced into the dissipation equation without altering its performance in parallel shear flows. While the inclusion of this parameter may improve the prediction of the near wake, it will have no direct influence downstream. As was mentioned above, however, the spreading rate of the far wake will be largely determined by the dissipation equation. Thus a more general relation than the linearity assumed between the rate-of-strain invariant and the net source of dissipation may serve to improve the predictions throughout the flow.

6. Conclusions

The main conclusions which can be extracted from the text are as follows.

(i) The elliptic form of the continuity equation and equations for two components of momentum and the rate of turbulence dissipation have been solved numerically together with equations for turbulence kinetic energy or the four Reynolds-stress equations: the solution algorithm can be arranged such that calculations with the five-equation turbulence model requires an increased computer run time of only 50 % and little extra storage.

(ii) For the round isothermal wake flows without recirculation considered, the turbulence model is less significant than the boundary condition assumed in the plane of the trailing edge of the solid body. The influence of the assumed V velocity profile is shown to be particularly large.

(iii) The mean velocity profiles of the plane isothermal wake were predicted accurately with all three turbulence models. The normal-stress predictions show model III to have a slight advantage over model II while model I is unsatisfactory in this respect.

(iv) For isothermal wake flows with recirculation, all models result in underestimation of the length of the recirculation region and of the rate of spread of the downstream wake. The latter discrepancy is particularly serious and appears to stem from incorrect calculation of dissipation in the recirculation region.

(v) For both wakes with and without recirculation, the Reynolds-stress closures provide reasonable predictions of the normal stress, but the advantages for the corresponding values of the mean velocity are small.

(vi) An improvement to the dissipation equation, to remove the deficiency indicated in (iv), is suggested. It requires the incorporation of a term based on the rotation and rate-of-strain invariants.

The authors are glad to acknowledge financial support from the Ministry of Defence and the understanding support of colleagues at the National Gas Turbine Establishment and Rolls-Royce (1971) Ltd. The computer program was developed from a version of the EASI program, made available by Professor D. B. Spalding.

Appendix

The following conventions are introduced so that the equations in Cartesian and cylindrical-polar co-ordinates may be written in a common form:

$$x = x_1, \quad y = x_2, \quad U = U_1, \quad V = U_2, \quad W = U_3,$$

$$r \equiv \begin{cases} 1 & \text{for Cartesian co-ordinates,} \\ y & \text{for cylindrical co-ordinates.} \end{cases}$$

Terms in curly brackets are to be included only in cylindrical co-ordinates.

Continuity equation

$$\frac{\partial}{\partial x}(\rho U)+\frac{1}{r}\frac{\partial}{\partial y}(r\rho V) = 0.$$

Momentum equations

$$\frac{\partial}{\partial x}(\rho U^2)+\frac{1}{r}\frac{\partial}{\partial y}(r\rho U V) = -\frac{\partial}{\partial x}(\rho\overline{u^2})-\frac{1}{r}\frac{\partial}{\partial y}(r\rho\overline{uv})-\frac{\partial p}{\partial x},$$

$$\frac{\partial}{\partial x}(\rho U V)+\frac{1}{r}\frac{\partial}{\partial y}(r\rho V^2) = -\frac{\partial}{\partial x}(\rho\overline{uv})-\frac{1}{r}\frac{\partial}{\partial y}(r\rho\overline{v^2})-\frac{\partial p}{\partial y}+\left\{\rho\frac{\overline{w^2}}{r}\right\}.$$

Model I

$$\frac{\partial}{\partial x}(\rho Uk)+\frac{1}{r}\frac{\partial}{\partial y}(r\rho Vk) = \frac{\partial}{\partial x}\left(\frac{\mu_{\text{eff}}}{\sigma_k}\frac{\partial k}{\partial x}\right)+\frac{1}{r}\frac{\partial}{\partial y}\left(r\frac{\mu_{\text{eff}}}{\sigma_k}\frac{\partial k}{\partial y}\right)+P-\rho\epsilon,$$

$$\frac{\partial}{\partial x}(\rho U\epsilon)+\frac{1}{r}\frac{\partial}{\partial y}(r\rho V\epsilon) = \frac{\partial}{\partial x}\left(\frac{\mu_{\text{eff}}}{\sigma_\epsilon}\frac{\partial \epsilon}{\partial x}\right)+\frac{1}{r}\frac{\partial}{\partial y}\left(r\frac{\mu_{\text{eff}}}{\sigma_\epsilon}\frac{\partial \epsilon}{\partial y}\right)+\frac{\epsilon}{k}(C_{\epsilon1}P-C_{\epsilon2}\rho\epsilon).$$

$$\mu_{\text{eff}} = \rho C_\mu k^2/\epsilon,$$

$$\rho\overline{uv} = -\mu_{\text{eff}}\left(\frac{\partial U}{\partial y}+\frac{\partial V}{\partial x}\right), \quad \rho\overline{u^2} = \tfrac{2}{3}\rho k-2\mu_{\text{eff}}\frac{\partial U}{\partial x},$$

$$\rho\overline{v^2} = \tfrac{2}{3}\rho k-2\mu_{\text{eff}}\frac{\partial V}{\partial y}, \quad \rho\overline{w^2} = \tfrac{2}{3}\rho k-\{2\mu_{\text{eff}}V/r\},$$

$$P = -\rho\left(\overline{uv}\left(\frac{\partial U}{\partial y}+\frac{\partial V}{\partial x}\right)+\overline{u^2}\frac{\partial U}{\partial x}+\overline{v^2}\frac{\partial V}{\partial y}+\{\overline{w^2}V/r\}\right).$$

Reynolds-stress models

$$\frac{\partial}{\partial x}(\rho U\overline{u^2})+\frac{1}{r}\frac{\partial}{\partial y}(r\rho V\overline{u^2}) = D(C_s\overline{u^2})+P_{11}+R_{11}-\tfrac{2}{3}\rho\epsilon,$$

$$\frac{\partial}{\partial x}(\rho U\overline{v^2})+\frac{1}{r}\frac{\partial}{\partial y}(r\rho V\overline{v^2}) = D(C_s\overline{v^2})+P_{22}+R_{22}-\tfrac{2}{3}\rho\epsilon-\left\{2\rho\frac{C_s k\overline{w^2}}{\epsilon}\frac{(\overline{v^2}-\overline{w^2})}{r^2}\right\},$$

$$\frac{\partial}{\partial x}(\rho U\overline{w^2})+\frac{1}{r}\frac{\partial}{\partial y}(r\rho V\overline{w^2}) = D(C_s\overline{w^2})+P_{33}+R_{33}-\tfrac{2}{3}\rho\epsilon+\left\{2\rho\frac{C_s k\overline{w^2}}{\epsilon}\frac{(\overline{v^2}-\overline{w^2})}{r^2}\right\},$$

$$\frac{\partial}{\partial x}(\rho U\overline{uv})+\frac{1}{r}\frac{\partial}{\partial y}(r\rho V\overline{uv}) = D(C_s\overline{uv})+P_{12}+R_{12}-\left\{\rho\frac{C_s k\overline{w^2}}{\epsilon}\frac{\overline{uv}}{r^2}\right\},$$

$$\frac{\partial}{\partial x}(\rho U\epsilon)+\frac{1}{r}\frac{\partial}{\partial y}(r\rho V\epsilon) = D(C_\epsilon\epsilon)+\frac{\epsilon}{k}(C_{\epsilon1}P-C_{\epsilon2}\rho\epsilon),$$

$$D(\phi) = \frac{\partial}{\partial x}\frac{\rho k}{\epsilon}\left(\overline{u^2}\frac{\partial\phi}{\partial x}+\overline{uv}\frac{\partial\phi}{\partial y}\right)+\frac{1}{r}\frac{\partial}{\partial y}\frac{\rho k}{\epsilon}\left(\overline{v^2}\frac{\partial\phi}{\partial y}+\overline{uv}\frac{\partial\phi}{\partial x}\right),$$

$$P_{11} = -2\rho\left(\overline{u^2}\frac{\partial U}{\partial x}+\overline{uv}\frac{\partial U}{\partial y}\right), \quad P_{22} = -2\rho\left(\overline{v^2}\frac{\partial V}{\partial y}+\overline{uv}\frac{\partial V}{\partial x}\right),$$

$$P_{33} = -\{2\rho\overline{w^2}V/r\}, \quad P_{12} = -\rho\left(\overline{v^2}\frac{\partial U}{\partial y}+\overline{u^2}\frac{\partial V}{\partial x}-\{\overline{uv}V/r\}\right).$$

Model II

$$R_{11} = -C_{\phi1}\rho\epsilon k^{-1}(\overline{u^2}-\tfrac{2}{3}k)-C_{\phi2}(P_{11}-\tfrac{2}{3}P),$$

$$R_{22} = -C_{\phi1}\rho\epsilon k^{-1}(\overline{v^2}-\tfrac{2}{3}k)-C_{\phi2}(P_{22}-\tfrac{2}{3}P),$$

$$R_{33} = -C_{\phi1}\rho\epsilon k^{-1}(\overline{w^2}-\tfrac{2}{3}k)-C_{\phi2}(P_{33}-\tfrac{2}{3}P),$$

$$R_{12} = -C_{\phi1}\rho\epsilon k^{-1}\overline{uv}-C_{\phi2}P_{12}.$$

Model III

$$\begin{aligned} R_{11} = {} & -C_{\phi1}\rho\epsilon k^{-1}(\overline{u^2}-\tfrac{2}{3}k)-B_1(P_{11}-\tfrac{2}{3}P) \\ & -2B_2\rho k\frac{\partial U}{\partial x}+2B_3\left(\rho\overline{u^2}\frac{\partial U}{\partial x}+\rho\overline{uv}\frac{\partial V}{\partial x}+\tfrac{1}{3}P\right), \end{aligned}$$

$$\begin{aligned} R_{22} = {} & -C_{\phi1}\rho\epsilon k^{-1}(\overline{v^2}-\tfrac{2}{3}k)-B_1(P_{22}-\tfrac{2}{3}P) \\ & -2B_2\rho k\frac{\partial V}{\partial y}+2B_3\left(\rho\overline{v^2}\frac{\partial V}{\partial y}+\rho\overline{uv}\frac{\partial U}{\partial y}+\tfrac{1}{3}P\right), \end{aligned}$$

$$\begin{aligned} R_{33} = {} & -C_{\phi1}\rho\epsilon k^{-1}(\overline{w^2}-\tfrac{2}{3}k)-B_1(P_{33}-\tfrac{2}{3}P) \\ & -\{2B_2\rho kV/r\}+2B_3\left(\left\{\rho\frac{\overline{w^2v}}{r}\right\}+\tfrac{1}{3}P\right), \end{aligned}$$

$$\begin{aligned} R_{12} = {} & -C_{\phi1}\rho\epsilon k^{-1}\overline{uv}-B_1P_{12}-B_2\rho k\left(\frac{\partial U}{\partial y}+\frac{\partial V}{\partial x}\right) \\ & +B_3\rho\left(\overline{u^2}\frac{\partial U}{\partial y}+\overline{v^2}\frac{\partial V}{\partial x}+\overline{uv}\left[\frac{\partial U}{\partial x}+\frac{\partial V}{\partial y}\right]\right). \end{aligned}$$

REFERENCES

BRADSHAW, P. 1973 Effects of streamline curvature on turbulent flow. *AGARDograph*, no. 169.

CARMODY, T. 1964 Establishment of the wake behind a disk. *A.S.M.E. J. Basic Engng*, **86**, 869.

CHEVRAY, R. 1968 The turbulent wake of a body of revolution. *A.S.M.E. J. Basic Engng*, **90**, 275.

CHEVRAY, R. & KOVASZNAY, L. S. G. 1969 Turbulence measurements in the wake of a thin flat plate. *A.I.A.A. J.* **7**, 1641.

DURÃO, D. F. G. & WHITELAW, J. H. 1974 *Proc. Laser Velocimeter Workshop. Purdue University*, **2**, 413.

GOSMAN, A. D., PUN, W. M., RUNCHAL, A. K., SPALDING, D. B. & WOLFSHTEIN, M. 1968 *Heat and Mass Transfer in Recirculating Flows*. Academic.

KHALIL, E. & WHITELAW, J. H. 1974 The calculation of local flow properties in two-dimensional furnaces. *Imperial College, Dept. Mech. Engng Rep.* HTS/74/38.

KLEBANOFF, P. S. 1954 Characteristics of turbulence in a boundary layer with zero pressure gradient. *N.A.C.A. Tech. Note*, no. 3178.

LAUNDER, B. E., MORSE, A., RODI, W. & SPALDING, D. B. 1972 The prediction of free shear flows – a comparison of the performance of six turbulence models. *N.A.S.A.* SP–311, p. 361.

LAUNDER, B. E., REECE, G. J. & RODI, W. 1975 Progress in the development of a Reynolds-stress turbulence closure. *J. Fluid Mech.* **68**, 537.

LAUNDER, B. E. & SPALDING, D. B. 1972 *Mathematical Models of Turbulence*. Academic.

NAOT, D., SHAVIT, A. & WOLFSHTEIN, M. 1970 Interaction between components of the turbulent velocity correlation tensor. *Israel J. Tech.* **8**, 259.

PATANKAR, S. V. & SPALDING, D. B. 1973 A calculation procedure for heat, mass and momentum transfer in three-dimensional parabolic flows. *Int. J. Heat. Mass Transfer*, **15**, 1787.

POPE, S. B. 1975 A more general effective-viscosity hypothesis. *J. Fluid Mech.* **72**, 331.

RODI, W. 1972 The prediction of free turbulent boundary layers by use of a two-equation model of turbulence. Ph.D. thesis, University of London.

ROTTA, J. C. 1951 Statistische Theorie Nichthomogener Turbulenz. *Z. Phys.* **129**, 547.